Development and Characteristic Investigation of a Multidimensional Discrete Magnetostrictive Actuator

Long Chen, Yuchuan Zhu, Jie Ling, *Member, IEEE*, and Mingming Zhang

***Abstract*—Active combustion control (ACC) has been proved to be an effective method for the suppression of pressure oscillation in aero engine combustion chambers, which will seriously endanger flight safety of aircrafts. However, the actuators for ACC need to work with a bandwidth of 1000 Hz, a stroke up to submillimeter level and a high power density simultaneously. Existing electromagnetic actuators, or smart material actuators, are still unable to meet these requirements at the same time. To address this issue, in this article, a multidimensional discrete magnetostrictive actuator (MDMA) was developed by adopting the multidimensional discrete configuration. In order to obtain large output displacement while maintaining the characteristics of high bandwidth and high power density of magnetostrictive materials, tubular and cylindrical magnetostrictive rods are nested axially and radially through sleeves to form a discrete magnetostrictive stack; independent excitation coils and permanent magnet rings are integrated axially to form a discrete electromagnetic excitation system. Then, a magnetic equivalent circuit (MEC) model was developed to analyze the magnetic field distribution characteristic of MDMA components. Next, a multiphysics comprehensive dynamic model was established to describe the complex dynamic properties of multidimensional discrete structures. Subsequently, a prototype of the MDMA was fabricated, which is only 56 mm in diameter and only 71.5 mm high. Experimental results indicate that, the proposed MDMA reaches a stoke of 100 μm, and the working bandwidth can exceed 1000 Hz. Furthermore, closed-loop control tests were conducted and the results showed that the MDMA can effectively track sinusoidal references of different amplitudes under low frequency with a feedback PID controller.**

***Index Terms*—High bandwidth, high power density, large stroke, magnetostrictive actuator (MA), multidimensional discrete configuration.**

I. Introduction

WITH the development of modern aero-engines, low emission, and high efficiency become two critical requirements [1], especially in civil aviation [2]. Many compelling evidences indicate that, lean combustion technology that has been widely used in aero-engines is feasible to save energy and reduce emissions [3], [4]. However, an inherent detrimental effect of this technology is combustion instability, which has a specific manifestation of pressure oscillation in the combustion chamber [5], [6]. If these pressure fluctuations are not mitigated, the stability and safety of aero-engine will be seriously diminished [7].

At present, active combustion control (ACC) technology has been proved to be an effective approach to suppress the combustor pressure oscillation [8], [9]. The specific operation of ACC is realized by real-time adjustment of fuel flow [10]–[12]. For a traditional ACC system, it usually consists of sensors, controllers and actuators, as shown in Fig. 1. Research works on sensing systems and control systems for ACC of aero-engines have been extensively carried out and has obtained remarkable achievements [13]–[15]. However, the research on the actuator system lags far behind. One of the leading factors is that, the frequency of pressure oscillating wave in the combustion chamber is up to 1000 Hz [16]. So the ACC will puts forward higher requirements on the bandwidth of the fuel regulator, which is responsible for the fuel flow regulation of aero engines [17], [18]. This exceeds the limit of traditional electromagnetic actuators that drive the regulators [12]. Nabae *et al.* [19] proposed an electromagnetic actuator, the bandwidth of which is only 300 Hz. Guo *et al.* [20] carried out the optimization work of electromagnetic actuators to improve its frequency response. Experiments show that the bandwidth of the optimized actuator can only reach 350 Hz.

Standing on the opposite of electromagnetic actuators, smart material based actuators, mainly includes piezoelectric actuators (PA) and magnetostrictive actuators (MAs), have caught a lot of attentions in aviation depend on their characteristics of high working bandwidth and high energy density [21]–[23]. Although the PA has a smaller volume and simpler structure [24], [25],

Manuscript received 28 December 2021; revised 18 March 2022 and 28 April 2022; accepted 30 April 2022. Date of publication 19 May 2022; date of current version 16 August 2022. This work was supported in part by the National Natural Science Foundation of China under Grant 51975275, in part by the Postgraduate Research and Practice Innovation Program of Jiangsu Province under Grant KYCX21_0195, and in part by the Primary Research and Development Plan of Jiangsu Province under Grant BE2021034. Recommended by Technical Editor T. Shimono and Senior Editor X. Chen. *(Corresponding authors: Yuchuan Zhu; Jie Ling.)*

The authors are with the National Key Laboratory of Science and Technology on Helicopter Transmission, Nanjing University of Aeronautics and Astronautics, Nanjing 210016, China (e-mail: meelongchen@nuaa.edu.cn; meeyczhu@nuaa.edu.cn; meejling@nuaa.edu.cn; mmingZ@nuaa.edu.cn).

Color versions of one or more figures in this article are available at https://doi.org/10.1109/TMECH.2022.3173619.

Digital Object Identifier 10.1109/TMECH.2022.3173619

constrained by piezoelectric material's low curie temperature and electrical breakdown hidden trouble, the requirements of aero-engine for high-operating temperature and high reliability of actuator cannot be met temporarily. So, MA is more promising, because: 1) magnetostrictive materials have a higher curie temperature (380 °C, commercially available), 2) magnetostrictive materials are driven by magnetic field in a contactless way, which makes their reliability is more superior than piezoelectric materials. But restricted by magnetostrictive material's magnetostrain rate, which is usually less than 0.2%, the traditional MA cannot get enough output stroke in a relatively small weight and volume. The suppression degree of combustor pressure oscillation is directly decided by the stroke of the actuator. Delaat *et al.* [16] developed a high bandwidth fuel regulator based on magnetostrictive material. The bandwidth of which is up to 600 Hz and the stroke is up to 0.38 mm. However, in order to achieve this stroke, the external size of the actuator reaches 0.46 m. This is intolerable, because for aero engines, power-to-weight ratio and power-to-volume ratio are critical parameters for evaluating its performance.

Therefore, the amplification of micro displacement by adopting amplification mechanism has been widely concerned in recent years. Regrettably, although displacement amplification actuators can obtain sufficient stroke in a small volume, the addition of displacement amplification mechanism will greatly sacrifice the bandwidth of the actuator [26], [27]. No matter the flexible hinge displacement amplification mechanism proposed by Tian *et al.* [28], the hydraulic displacement amplification mechanism designed by Yang *et al.* [29], or the lever displacement amplification mechanism established by Bartlett *et al.* [30], while realizing the displacement amplification, the bandwidth is reduced by more than 70%.

As mentioned above, the existing actuator design schemes cannot simultaneously meet the requirements of high bandwidth, large stroke, and high power density in the actual application of ACC for aero engines. There is another effective method to realize displacement amplification by designing a special stack configuration. In our previous work [31], a novel radially discrete stack configuration was proposed. By radial stacking of two tubular and one cylindrical magnetostrictive rods, a stroke of 65 μm is achieved under an axial dimension of 69 mm and a weight of 1548 g, the bandwidth is kept as 500 Hz, which shows a broad prospect in ACC of aero-engines.

In this article, based on the radially discrete stack configuration, a novel multidimensional discrete configuration for MAs is proposed. In the configuration, the magneto-mechanical conversion system, the electromagnetic excitation system and the magnetic bias system of the MA are all discretized:

1) an axial-radial discrete magnetostrictive stack is designed to increase the stroke and keep the high bandwidth;
2) an axial discrete excitation coil is developed to improve the motion control accuracy and bandwidth of the actuator;
3) an axial discrete magnetic bias system with annular permanent magnet is designed to provide bias magnetic field, reduce mass and volume of the actuator and improve work efficiency.

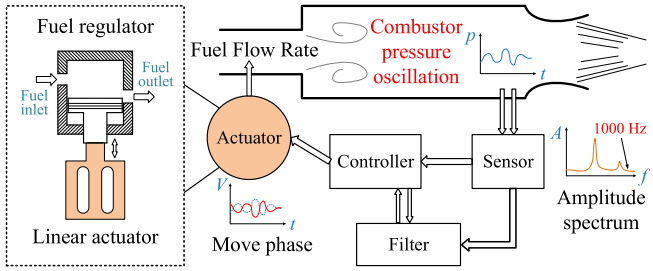

Fig. 1. ACC system. The fuel regulator needs to operate at a bandwidth of 1000 Hz.

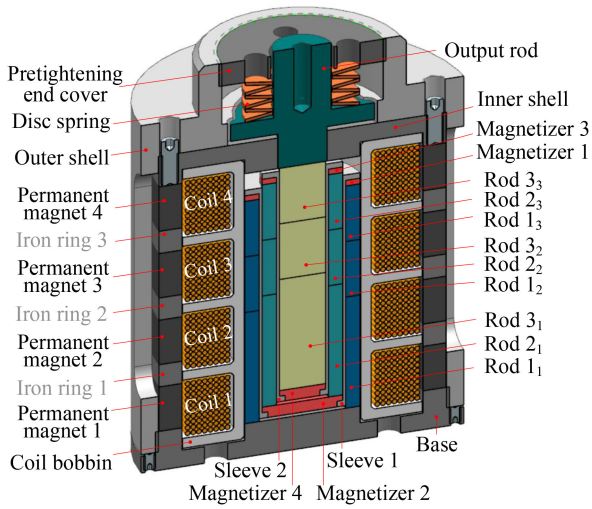

Fig. 2. Structure of the proposed MDMA.

Finally, a multidimensional discrete magnetostrictive actuator (MDMA) is developed, and a prototype is fabricated. Experimental results show that the MDMA can output a displacement of 100 μm under an axial size of 71.5 mm and a radial size of 56 mm, and its weight is 787 g, bandwidth can exceed 1000 Hz.

The rest of this article is organized as follows. The structure and working principle of the proposed MDMA is introduced in Section II. The analysis and modeling of the MDMA magnetic circuit is carried out in Section III. In Section IV, a dynamic model of the MDMA is established. In Section V, a prototype of the proposed MDMA is fabricated and a series of performance testing experiments are carried out. Finally, Section VI concludes this article.

II. Structure and Working Principle of the MDMA

A. Structure of the MDMA

The output displacement amplitude of MA is affected by many factors, including stack length, magnetic field intensity, and preload strength. Therefore, like traditional MAs, the MDMA consists of the following three parts: the magnetostrictive stack, the electromagnetic excitation section, and the preload application mechanism. As shown in Fig. 2, the magnetostrictive

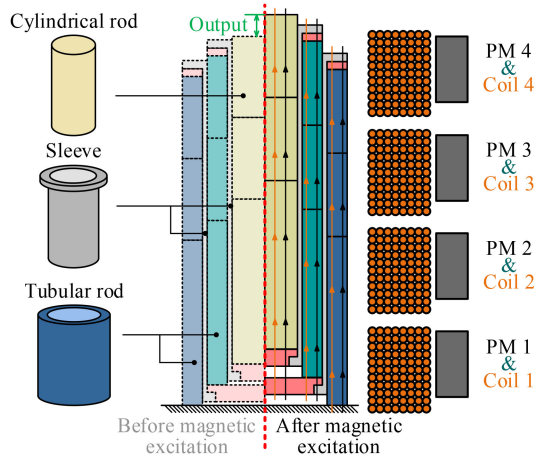

Fig. 3. Multidimensional discrete configuration. In which, orange field lines represent the excitation field generated by coils and black field lines represent the offset field generated by the permanent magnets.

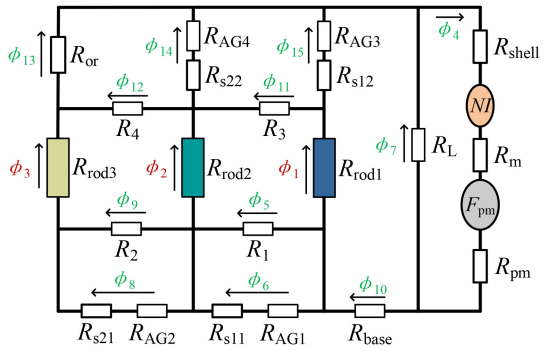

Fig. 4. MEC model of the MDMA. In which, NI and $F_{\rm pm}$ represent the excitation and bias magnetomotive force generated by excitation coils and permanent magnets, respectively; ϕ_1 to ϕ_{15} are the magnetic flux; $R_{\rm rod1}$, $R_{\rm rod2}$, and $R_{\rm rod3}$ represent the magnetic reluctance of rod 1, rod 2, and rod 3, respectively; $R_{\rm shell}$, $R_{\rm or}$, $R_{\rm base}$, R_m, and $R_{\rm pm}$ are the magnetic reluctance of inner shell, output rod, base, iron rings, and permanent magnets, respectively; R_{s11}, R_{s12}, R_{s21}, and R_{s22} are the magnetic reluctance of magnetizer 2, magnetizer 1, magnetizer 4, and magnetizer 3, respectively; R_L is the leakage magnetic reluctance; R_1 to R_4 are the radial transfer magnetic reluctance; $R_{\rm AG1}$ to $R_{\rm AG4}$ are the air gaps magnetic reluctance.

stack of the MDMA consist of nine Terfenol-D rods those are responsible for magneto-machine conversion and two sleeves, which are responsible for the transfer of displacement; the electromagnetic excitation section consist of four independent coils, which are responsible for electromagnetic conversion and four circular permanent magnets those are responsible for the generation of bias magnetic field; the preload application mechanism consists of disc springs and is responsible for applying preload.

B. Working Principle of the MDMA

As shown in Fig. 3, the multidimensional discrete configuration mainly includes the following three parts: axial-radial discrete magnetostrictive stack, radially discrete electromagnetic excitation coil, and radially discrete permanent magnets.

Sufficient output displacement can be obtained only by increasing axial length or adding additional amplification mechanism for traditional MAs. In contrast, the MDMA achieves displacement amplification by employing the radial nested stack structure. In the MDMA, the axial-radial discrete magnetostrictive stack consists of three-stage magnetostrictive rods in both radial and axial directions, when excited by an external magnetic field, all the magnetostrictive rods deform simultaneously and output their displacement along the axial direction. The sleeve transmits the displacement of the outer tubular magnetostrictive rod radially inward, and finally converges to the top of the innermost cylindrical magnetostrictive rod, which becomes the total output displacement of the magnetostrictive stack. The high bandwidth and high energy density of magnetostrictive materials can be preserved by this discrete stack structure while achieving displacement amplification. Because on the one hand, no additional amplification mechanism is introduced, on the other hand, axial size of the stack is not increased.

The electromagnetic excitation system mainly determines the bandwidth and power density of the MA. In the radial discrete electromagnetic excitation system, the circular permanent magnet is used to provide bias magnetic field, which can greatly reduce the number of turns of the excitation coil and improve the electromagnetic conversion efficiency and power density; the inductive reactance of the excitation coil is reduced through the dispersion of the excitation coil and the frequency response of the electromagnetic conversion process is improved.

III. Magnetic Circuit Model of the MDMA

A. Establishment of the Magnetic Equivalent Circuit (MEC) Model

One of the by-products of the multidimensional discrete configuration is the uneven magnetic field distribution. In order to accurately analyze the internal magnetic field distribution of MDMA, the MEC model was established, as shown in Fig. 4, rod 1_1, rod 1_2, and rod 1_3 are considered to be a holistic magnetostrictive rod 1, the same goes for rod 2 and rod 3. According to Kirchhoff's law, the MEC model can be described by (16) in Appendix A.

B. Parameter Identification of the MEC Model

In the MDMA, the magnetic reluctance of some regular shape components can be obtained by numerical calculation or finite-element calculation. However, for air gap magnetic reluctance without specific shape and size, it can only be identified according to the finite element simulation results. The magnetic reluctance parameters in the MEC model are shown in Table I, in which $R_{\rm pm}$, R_L, $R_{\rm AG3}$, $R_{\rm AG4}$, R_1, R_2, R_3, and R_4 are obtained by identification. The simulation results of the finite element model (FEM) and the calculation results of MEC model are compared in Fig. 5, which indicate that the established MEC

TABLE I
PARAMETERS OF THE MEC MODEL

Symbol	Value (H^{-1})	Symbol	Value (H^{-1})
R_{shell}	5.34×10^3	R_{L}	9.13×10^8
R_{base}	5.23×10^3	R_1	1.81×10^7
R_{or}	1.50×10^3	R_2	2.34×10^7
R_{rod1}	4.63×10^7	R_3	4.11×10^6
R_{rod2}	7.05×10^7	R_4	3.20×10^6
R_{rod3}	1.27×10^8	R_{AG1}	2.25×10^6
R_{s11}	865.4	R_{AG2}	6.25×10^6
R_{s12}	484.6	R_{AG3}	2.37×10^7
R_{s21}	2.65×10^3	R_{AG4}	7.40×10^8
R_{s22}	737.5	R_{pm}	1.88×10^6
R_{m}	1.39×10^3	-	-

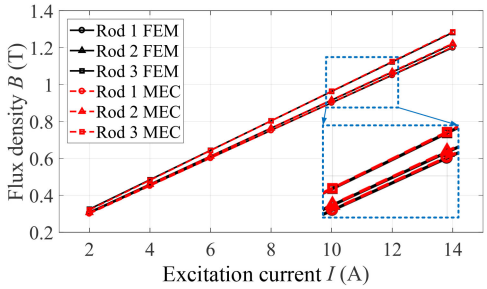

Fig. 5. Accuracy verification of the established MEC model.

model can accurately describe the heterogeneous magnetic paths of MDMA.

IV. DYNAMIC MODEL OF THE MDMA

In the working process of MDMA, the excitation coil is responsible for converting current into a magnetic field to magnetize the magnetostrictive rods. After magnetization, the magnetostrictive rod's internal magnetic domain is deflected, resulting in magnetostrictive force. Then, the magnetostrictive rods extend and push sleeves, magnetizers and output rod, and finally, becomes the output displacement of the MDMA.

A. Nonlinear Dynamic Magnetization Model

According to the established MEC model, the magnetic flux of each magnetostrictive rod can be calculated as follows:

$$\boldsymbol{\phi} = A^{-1}B. \tag{1}$$

The matrix $\boldsymbol{\phi}$, $\boldsymbol{A}$, and $\boldsymbol{B}$ are shown in (17) in Appendix B, in which, F_T, $R_{9,15}$, $R_{11,6}$, $R_{13,8}$, $R_{14,14}$, $R_{15,14}$, and $R_{15,15}$ can be calculated as

$$\begin{cases} R_{9,15} = R_{s12} + R_{\text{AG3}}, \quad R_{11,6} = R_{s11} + R_{\text{AG1}} \\ R_{13,8} = R_{s21} + R_{\text{AG2}}, \quad R_{14,14} = R_{s22} + R_{\text{AG4}} \\ R_{15,14} = R_{s22} + R_{\text{AG4}}, \quad R_{15,15} = R_{s12} + R_{\text{AG3}} \\ R_{8,4} = R_{\text{shell}} + R_m + R_{\text{pm}}, \quad F_T = \text{NI} + F_{\text{pm}} \end{cases}. \tag{2}$$

Taking eddy current effects into account, magnetic field strength of each magnetostrictive rod can be expressed as [32]

$$\begin{cases} H = H_c - H' = \frac{\phi}{k_f \mu A} - \int_{\frac{d_i}{2}}^{\frac{d_0}{2}} r \mathrm{d}r \frac{\mu_0 \mu_G}{2 k_J \rho_G} \frac{dH_c}{dt} \\ H(s) = \frac{\phi}{k_f \mu A \left(1 + \frac{\mu_0 \mu_G (d_o^2 - d_i^2)}{16 k_J \rho_G} s\right)} \end{cases} \tag{3}$$

where H_c is the magnetic intensity generated by the excitation coil; H' is the magnetic intensity generated by the eddy current; ϕ is the magnetic flux; μ is the permeability; A is the cross-sectional area; μ_0 is the vacuum permeability; μ_G is the relative permeability of the magnetostrictive rod; d_o and d_i are the outer and inner diameter of the magnetostrictive rod; ρ_G is the resistivity of the magnetostrictive rod; k_f and k_J are the magnetic flux leakage compensation factor, and the eddy current effect compensation factor, respectively.

The magnetization of magnetostrictive rods can be calculated by Jiles–Atherton (J-A) model, which is the most widely used magnetization model, as the following five equations [31]:

$$\begin{cases} H_e = H + \alpha M \\ M_{\text{ir}} = M_{\text{an}} - k\delta\left(\frac{dM_{\text{ir}}}{dH_e}\right) \\ M = M_r + M_{\text{ir}} \\ M_{\text{an}} = M_s\left[\coth\left(\frac{H_e}{a}\right) - \frac{a}{H_e}\right] \\ M_r = c_r(M_{\text{an}} - M_{\text{ir}}) \end{cases} \tag{4}$$

where H_e is the effective magnetic field, α is the magnetic domain interaction coefficient, M is the magnetization, M_{ir} is the magnetization's irreversible value, M_{an} is an hysteretic value of magnetization, k is the pinning coefficient, δ is the directional coefficient, M_r is the reversible value of magnetization, M_s is the saturation magnetization, a is the shape coefficient of the magnetization curve without hysteresis, and c_r is the reversible coefficient.

B. Magnetostrictive Force Model

The internal magnetic domains of a magnetostrictive rod will deflect under the action of an external magnetic field, which will produce magnetostrictive strain, and then resulting in magnetostrictive force. The preload is one of the main factors that affects the strain of magnetostrictive rods, which can be expressed as [33]

$$\lambda = \begin{cases} \left(1 + \frac{1}{2}\tanh\frac{2F_p}{F_s}\right)\lambda_s \frac{M^2}{M_s^2}, & F_p \le F_s \\ \left(1 - \frac{F_p - F_s}{F_{\max}}\right)\left(1 + \frac{1}{2}\tanh\frac{2F_p}{F_s}\right)\lambda_s \frac{M^2}{M_s^2}, & F_p > F_s \end{cases} \tag{5}$$

where λ is the magnetostrictive strain, F_p is the preload of a magnetostrictive rod, F_s is the saturation preload, λ_s is the saturation magnetostrictive strain, M is the magnetization intensity, and $F_{\max}$ is the maximum magnetostrictive force.

The output force F of magnetostrictive rods can be calculated by the following equation [33]:

$$F = \lambda E_G A_G \tag{6}$$

where E_G and A_G are the elastic modulus and the cross-sectional area of a magnetostrictive rod, respectively.

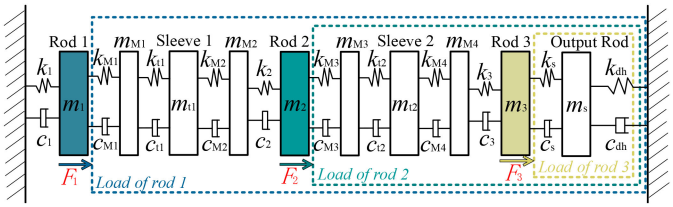

Fig. 6. Schematic of the MDOF dynamic model.

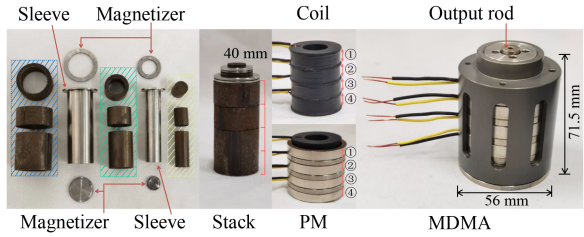

Fig. 7. Prototype of the MDMA. Magnetizers, iron rings, inner shell, base, and output rod are made of DT4C; sleeves and pretightening end cover are made of SUS304; outer shell is made of aluminum alloy 7075; coil bobbin is made of polycarbonate; permanent magnet is made of NbFeB.

C. Multidegree-of-Freedom (MDOF) Mechanical Dynamic Model

In the MDMA, all components form an MDOF dynamic system in which magnetostrictive rods become force sources, sleeves, magnetizers, and output rod responsible for the transfer of force and displacement, as shown in Fig. 6. For each magnetostrictive rod, in addition to overcoming its own mass, stiffness, and damping, it should also overcome the mass, stiffness, and damping of other components in the output direction. The establishment of MDOF mechanical dynamic model is of great significance for guiding the design and optimization of the MDMA.

The dynamic equation of the system can be expressed as

$$M\ddot{X} + C\dot{X} + KX = F \tag{7}$$

the matrix $\boldsymbol{M}$, $\boldsymbol{C}$, $\boldsymbol{K}$, $\boldsymbol{X}$, and $\boldsymbol{F}$ can be expressed as follows:

$$M = \begin{bmatrix} \frac{m_1}{3} + m_{\mathrm{lr}1} & 0 & 0 \\ 0 & \frac{m_2}{3} + m_{\mathrm{lr}2} & 0 \\ 0 & 0 & \frac{m_3}{3} + m_{\mathrm{lr}3} \end{bmatrix} \tag{8}$$

$$C = \begin{bmatrix} c_1 + c_{\mathrm{lr}1} & 0 & 0 \\ 0 & c_2 + c_{\mathrm{lr}2} & 0 \\ 0 & 0 & c_3 + c_{\mathrm{lr}3} \end{bmatrix} \tag{9}$$

$$K = \begin{bmatrix} k_1 + k_{\mathrm{lr}1} & 0 & 0 \\ 0 & k_2 + k_{\mathrm{lr}2} & 0 \\ 0 & 0 & k_3 + k_{\mathrm{lr}3} \end{bmatrix} \tag{10}$$

$$X = \begin{bmatrix} x_1 \\ x_2 \\ x_3 \end{bmatrix}, \; F = \begin{bmatrix} F_1 \\ F_2 \\ F_3 \end{bmatrix} \tag{11}$$

where m_1 to m_3, c_1 to c_3, k_1 to k_3, x_1 to x_3, and F_1 to F_3 are the mass, the damping, the stiffness, the output displacement, and the output force of rod 1, rod 2, and rod 3 respectively; $m_{\mathrm{lr}1}$ to $m_{\mathrm{lr}3}$, $c_{\mathrm{lr}1}$ to $c_{\mathrm{lr}3}$, and $k_{\mathrm{lr}1}$ to $k_{\mathrm{lr}3}$ are the equivalent load mass, the equivalent load damping, and the equivalent load stiffness of rod 1, rod 2, and rod 3, respectively, which can be calculated by the following equations:

$$\begin{cases} m_{\mathrm{lr}1} = \sum_{i=1}^{4} m_{\mathrm{Mi}} + m_{t1} + m_2 + m_{t2} + m_3 + m_s \\ m_{\mathrm{lr}2} = m_{M3} + m_{t2} + m_{M4} + m_3 + m_s \\ m_{\mathrm{lr}3} = m_s \end{cases} \tag{12}$$

$$\begin{cases} c_{\mathrm{lr}1} = \left(\sum_{i=1}^{4} \frac{1}{c_{\mathrm{Mi}}} + \frac{1}{c_{t1}} + \frac{1}{c_2} + \frac{1}{c_{t2}} + \frac{1}{c_3} + \frac{1}{c_s} + \frac{1}{c_{\mathrm{dh}}} \right)^{-1} \\ c_{\mathrm{lr}2} = \left(\frac{1}{c_{M3}} + \frac{1}{c_{t2}} + \frac{1}{c_{M4}} + \frac{1}{c_3} + \frac{1}{c_s} + \frac{1}{c_{\mathrm{dh}}} \right)^{-1} \\ c_{\mathrm{lr}3} = \left(\frac{1}{c_s} + \frac{1}{c_{\mathrm{dh}}} \right)^{-1} \end{cases} \tag{13}$$

$$\begin{cases} k_{\mathrm{lr}1} = \left(\sum_{i=1}^{4} \frac{1}{k_{\mathrm{Mi}}} + \frac{1}{k_{t1}} + \frac{1}{k_2} + \frac{1}{k_{t2}} + \frac{1}{k_3} + \frac{1}{k_s} + \frac{1}{k_{\mathrm{dh}}} \right)^{-1} \\ k_{\mathrm{lr}2} = \left(\frac{1}{k_{M3}} + \frac{1}{k_{t2}} + \frac{1}{k_{M4}} + \frac{1}{k_3} + \frac{1}{k_s} + \frac{1}{k_{\mathrm{dh}}} \right)^{-1} \\ k_{\mathrm{lr}3} = \left(\frac{1}{k_s} + \frac{1}{k_{\mathrm{dh}}} \right)^{-1} \end{cases} \tag{14}$$

where m_{M1} to m_{M4}, m_{t1}, m_{t2}, and m_s are the mass of magnetizer 1 to magnetizer 4, sleeve 1, sleeve 2, and output rod, respectively; c_{M1} to c_{M4}, c_{t1}, c_{t2}, c_s, and c_{dh} are the damping of magnetizer 1 to magnetizer 4, sleeve 1, magnetizer 2, sleeve 2, output rod, and disc spring, respectively; k_{M1} to k_{M4}, k_{t1}, k_{t2}, k_s, and k_{dh} are the stiffness of magnetizer 1 to magnetizer 4, sleeve 1, sleeve 2, output rod, and disc spring, respectively.

Finally, the state-space model of the MDOF dynamic system can be established as follows:

$$\begin{cases} \begin{bmatrix} \dot{X} \\ \ddot{X} \end{bmatrix} = \begin{bmatrix} \mathbf{0} & \mathbf{1} \\ -M^{-1}K & -M^{-1}C \end{bmatrix} \begin{bmatrix} X \\ \dot{X} \end{bmatrix} + \begin{bmatrix} \mathbf{0} \\ M^{-1} \end{bmatrix} F \\ Y = \begin{bmatrix} \mathbf{1} & \mathbf{0} \end{bmatrix} \begin{bmatrix} X \\ \dot{X} \end{bmatrix}. \end{cases} \tag{15}$$

V. Experimental Study of the MDMA

A. Prototype and Test Bench of the MDMA

As shown in Fig. 7, a prototype of the proposed MDMA was fabricated for the characteristic investigation. The magnetostrictive material employed in the prototype is Terfenol-D. Each magnetostrictive rod is composed of two 10 mm and one 20 mm rods with a total length of 40 mm. The excitation coil consists of four separate units, total number of turns is 720.

The test bench of the MDMA is shown in Fig. 8, in which four power amplifiers (AETechron Inc, 7224) are employed to drive discrete coils, the excitation current is measured by a current sensor (Shenzhen Zhiyong Co., Ltd, CP800), the output displacement of the MDMA is acquired by a capacitive displacement sensor (Harbin Core Tomorrow Technology Co.,

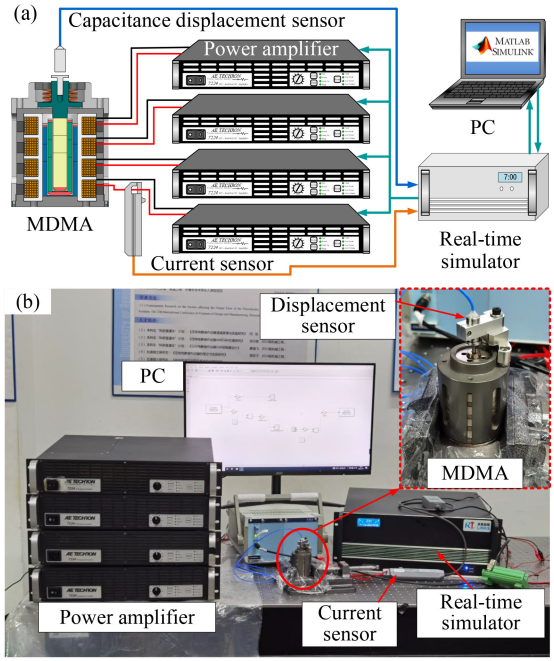

Fig. 8. Experimental platform for the MDMA. (a) Signal flow diagram. (b) composition of test bench.

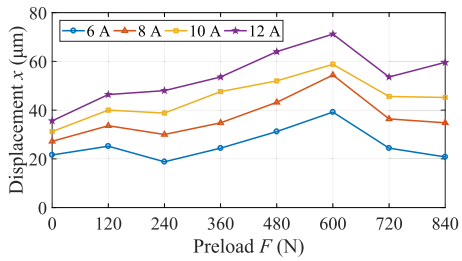

Fig. 9. Effect of preload.

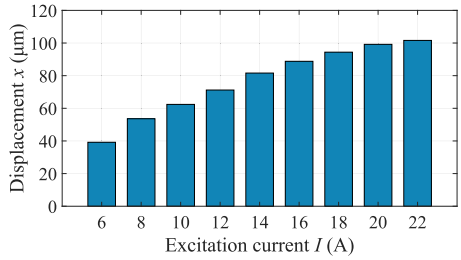

Fig. 10. Effect of excitation current.

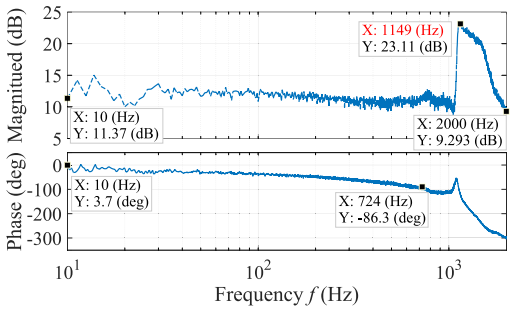

Fig. 11. Frequency response of MDMA.

TABLE II
COMPARISON BETWEEN THE PROPOSED MDMA AND OTHER WORKS

Studies	Type	Bandwidth (Hz)	Stroke (μm)	Volume (cm^3)	Weight (g)
Schiller, 2006 [24]	PA	800	300	N/A	N/A
Li, 2020 [25]	PA	1029	26.78	106.7	N/A
Chen, 2021 [31]	MA	500	65	273.2	1548
This work	MA	>1000*	100	163.1	787

* Experiment open-loop result, as shown in Fig. 11, while the closed-loop result is 367.5 Hz under step size of 50 μs, as shown in Fig. 14.

Ltd, E09.Cap), a real-time simulator (Beijing Lingsi Chuangqi Technology Co., LTD, Links-Box-03) is responsible for excitation signal generation and data acquisition simultaneously.

Due to the inherent frequency doubling effect, the excitation signal is a sinusoidal signal with a dc bias. The amplitude of the dc bias is determined by the strength of the bias field provided by the permanent magnets. According to the experimental results, the bias field provided by the permanent magnet in MDMA is the same as that generated by the coil under a excitation current of 2 A. Therefore, the dc bias must ensure that the low level of the excitation current is -2 A.

B. Open-Loop Performance of the MDMA

The output displacement of MDMA is mainly affected by preload and excitation current. As shown in Fig. 9, there is an optimal preload of 600 N for the MDMA. It can be seen from Fig. 10 that the MDMA has a saturation output displacement of 100 μm at the excitation current of 20 A. The frequency response of the MDMA is shown in Fig. 11, which indicate that the first-order natural frequency of the MDMA is 1149 Hz and the bandwidth of MDMA can exceed 1000 Hz.

The comparisons between the proposed MDMA and some previous studies are listed in Table II. Compared with the PA in [24] and [25], the proposed MDMA has a high bandwidth exceeding 1000 Hz and a stroke up to submillimeter level simultaneously. Compared with the actuator in our previous work [31], the proposed MDMA increased the stroke by 54% and bandwidth by 100% on the basis of 40% volume reduction and 49% mass reduction.

C. Parameter Identification of the Dynamic Model

In the MDMA dynamic model, there are some parameters that cannot be obtained by measurement or numerical calculation, such as α, k, a, and c_r in Jiles–Atherton model; damping parameters in mechanical dynamic model. They can only be identified experimentally. Multi-island genetic algorithm was employed to improve the accuracy of identification, and all parameters of the mechanical dynamic model are shown in Table III, parameters of the Jiles–Atherton model are shown in Table IV.

TABLE III
PARAMETERS OF DYNAMIC MODEL

Symbol	Unit	Value	Symbol	Unit	Value
m_1	g	50.9	k_{M3}	$N{\cdot}\mu m^{-1}$	2077
k_1	$N{\cdot}\mu m^{-1}$	103	c_{M3}	$N{\cdot}s{\cdot}m^{-1}$	3817
c_1	$N{\cdot}s{\cdot}m^{-1}$	5170	m_{t2}	g	5.3
m_{M1}	g	1.1	k_{t2}	$N{\cdot}\mu m^{-1}$	68.7
k_{M1}	$N{\cdot}\mu m^{-1}$	3161	c_{t2}	$N{\cdot}s{\cdot}m^{-1}$	1414
c_{M1}	$N{\cdot}s{\cdot}m^{-1}$	1295	m_{M4}	g	0.62
m_{t1}	g	8.9	k_{M4}	$N{\cdot}s{\cdot}m^{-1}$	506
k_{t1}	$N{\cdot}\mu m^{-1}$	117	c_{M4}	$N{\cdot}s{\cdot}m^{-1}$	3817
c_{t1}	$N{\cdot}s{\cdot}m^{-1}$	1414	m_3	g	18.6
m_{M2}	g	2.1	k_3	$N{\cdot}\mu m^{-1}$	37.7
k_{M2}	$N{\cdot}\mu m^{-1}$	939	c_3	$N{\cdot}s{\cdot}m^{-1}$	1257
c_{M2}	$N{\cdot}s{\cdot}m^{-1}$	3693	m_s	g	7.1
m_2	g	33.4	k_s	$N{\cdot}\mu m^{-1}$	642
k_2	$N{\cdot}\mu m^{-1}$	67	c_s	$N{\cdot}s{\cdot}m^{-1}$	8581
c_2	$N{\cdot}s{\cdot}m^{-1}$	776	k_{dh}	$N{\cdot}\mu m^{-1}$	0.31
m_{M3}	g	0.72	c_{dh}	$N{\cdot}s{\cdot}m^{-1}$	816

TABLE IV
PARAMETERS OF JILES–ATHERTON MODEL

Symbol	Unit	Rod1	Rod2	Rod3
M_s	$kA{\cdot}m^{-1}$	600	600	600
a	$A{\cdot}m^{-1}$	1484	8708	7012
α	—	–0.0014	–0.0234	–0.01
c_r	—	0.55	0.66	0.18
k	$A{\cdot}m^{-1}$	3475	4683	4283

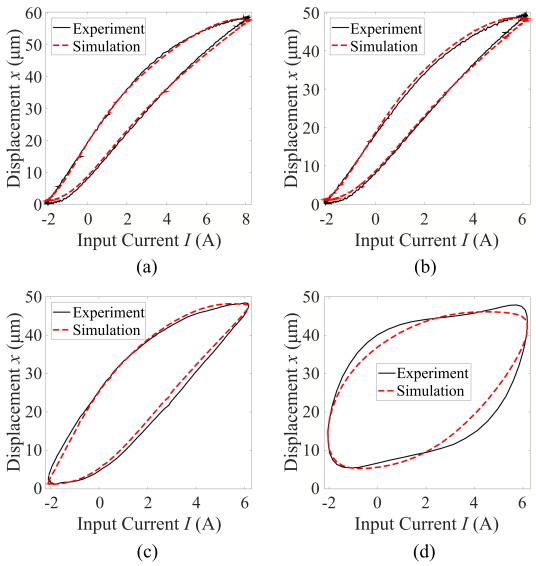

Fig. 12. Hysteresis diagram of the MDMA. (a) 10 A, 10 Hz. (b) 8 A, 10 Hz. (c) 8 A, 100 Hz. (d) 8 A, 400 Hz.

The output hysteresis diagram of MDMA at different working conditions is shown in Fig. 12. It can be seen that the hysteresis increases gradually as the frequency increases, the proposed dynamic model can accurately describe this property and the error is less than 5%.

D. Closed-Loop Test of the MDMA

To test the closed-loop performance of MDMA, an incremental PID controller is employed and parameters of which are tuned through experiments with the employment of the real-time

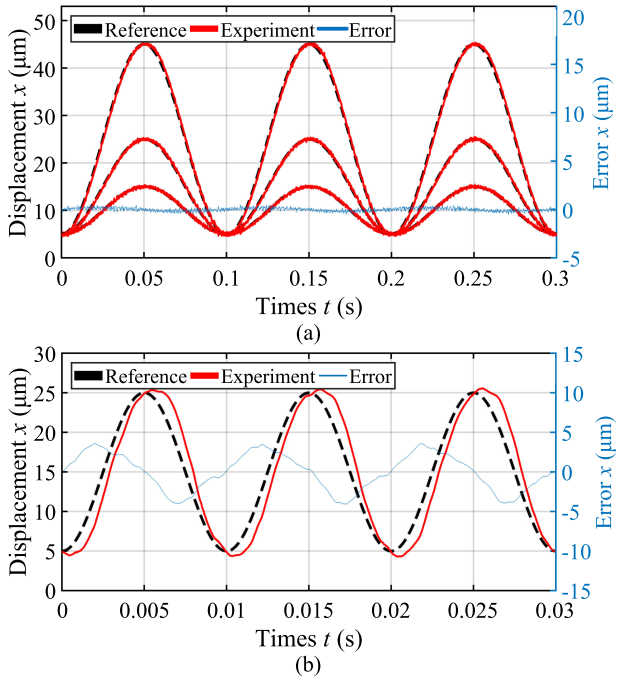

Fig. 13. Closed-loop test result of the MDMA. (a) 10 Hz. (b) 100 Hz.

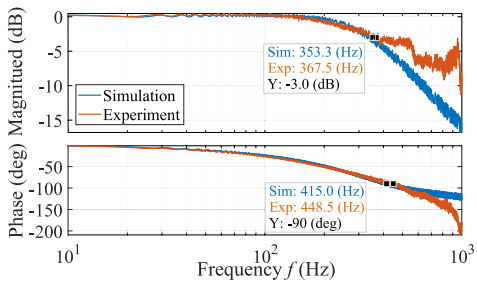

Fig. 14. Closed-loop frequency response of the MDMA under step size of 50 μs.

simulator. The criteria of parameter tuning is to minimize the root mean square (RMS) error and reduce oscillation in tracking target displacement. Under a sampling period of 50 μs, the parameters are set as $k_p = 0.2$, $k_i = 0.03$, and $k_d = 0.007$, respectively, to get the best control accuracy. As shown in Fig. 13, MDMA can effectively track reference with different amplitudes under 10 Hz, and the RMS error is less than 2%. However, the RMS error under 100 Hz reaches 11.53% and there is a time delay, which is mainly caused by the hysteresis of the actuator and displacement sensor. The closed-loop frequency response of the MDMA was measured though experiment and simulation, respectively, under a step size of 50 μs, in the simulation, the proposed dynamic model is employed. As shown in Fig. 14, the simulation results and experiment results have a high consistency in low frequency, and the closed-loop bandwidth of MDMA is $<$ 400 Hz. This mainly because the step size of 50 μs is not small enough for the closed-loop tracking under high frequency. In addition, a special controller should be designed further to ensure actuator closed-loop performance at high frequency.

$$A=\begin{bmatrix}
0 & 0 & 0 & -1 & 0 & 0 & 1 & 0 & 0 & 1 & 0 & 0 & 0 & 0 & 0\\
1 & 0 & 0 & 0 & 1 & 1 & 0 & 0 & 0 & -1 & 0 & 0 & 0 & 0 & 0\\
0 & 1 & 0 & 0 & -1 & -1 & 0 & 1 & 1 & 0 & 0 & 0 & 0 & 0 & 0\\
0 & 0 & 1 & 0 & 0 & 0 & 0 & -1 & -1 & 0 & 0 & 0 & 0 & 0 & 0\\
-1 & 0 & 0 & 0 & 0 & 0 & 0 & 0 & 0 & 0 & 1 & 0 & 0 & 0 & 1\\
0 & -1 & 0 & 0 & 0 & 0 & 0 & 0 & 0 & 0 & -1 & 1 & 0 & 1 & 0\\
0 & 0 & -1 & 0 & 0 & 0 & 0 & 0 & 0 & 0 & 0 & -1 & 1 & 0 & 0\\
0 & 0 & 0 & R_{8,4} & 0 & 0 & R_L & 0 & 0 & 0 & 0 & 0 & 0 & 0 & 0\\
R_{\mathrm{rod1}} & 0 & 0 & 0 & 0 & 0 & -R_{\mathrm{L}} & 0 & 0 & R_{\mathrm{base}} & 0 & 0 & 0 & 0 & R_{9,15}\\
-R_{\mathrm{rod1}} & R_{\mathrm{rod2}} & 0 & 0 & R_1 & 0 & 0 & 0 & 0 & 0 & -R_3 & 0 & 0 & 0 & 0\\
0 & 0 & 0 & 0 & -R_1 & R_{11,6} & 0 & 0 & 0 & 0 & 0 & 0 & 0 & 0 & 0\\
0 & -R_{\mathrm{rod2}} & R_{\mathrm{rod3}} & 0 & 0 & 0 & 0 & 0 & R_2 & 0 & 0 & -R_4 & 0 & 0 & 0\\
0 & 0 & 0 & 0 & 0 & 0 & 0 & R_{13,8} & -R_2 & 0 & 0 & 0 & 0 & 0 & 0\\
0 & 0 & 0 & 0 & 0 & 0 & 0 & 0 & 0 & 0 & 0 & R_4 & R_{\mathrm{or}} & -R_{14,14} & 0\\
0 & 0 & 0 & 0 & 0 & 0 & 0 & 0 & 0 & 0 & R_3 & 0 & 0 & R_{15,14} & -R_{15,15}
\end{bmatrix}\quad \boldsymbol{B}=\begin{bmatrix}0\\0\\0\\0\\0\\0\\0\\F_T\\0\\0\\0\\0\\0\\0\\0\end{bmatrix}\quad \boldsymbol{\phi}=\begin{bmatrix}\phi_1\\\phi_2\\\phi_3\\\phi_4\\\phi_5\\\phi_6\\\phi_7\\\phi_8\\\phi_9\\\phi_{10}\\\phi_{11}\\\phi_{12}\\\phi_{13}\\\phi_{14}\\\phi_{15}\end{bmatrix} \tag{17}$$

VI. Conclusion

In this article, in order to meet the requirements of aero-engine ACC for high-bandwidth, large-displacement, and high-power density actuators, an MDMA was developed. A MEC model and a dynamic model was developed to describe the magnetic field distribution and dynamic characteristics; a prototype was designed and fabricated and a series of experiments were carried out for the characteristic investigation of MDMA. The specific conclusions are as follows.

1) The established MEC model can describe the uneven distribution of magnetic fields within MDMA accurately, with an error less than 0.7%.
2) The proposed dynamic model can accurately describe the dynamic hysteresis nonlinearity of the MDMA, with an RMS error less than 5%.
3) The proposed MDMA have a stroke of 100 μm, and a bandwidth exceeding 1000 Hz, under a size of 56 mm$\times$71.5 mm.
4) MDMA can track sinusoidal references under 10 Hz of different amplitudes with an RMS error less than 2% with a feedback PID.

Appendix A

The MEC model of the MDMA can be described as follows:

$$\begin{cases}
\phi_7+\phi_{10}-\phi_4=0,\ \phi_1+\phi_5+\phi_6-\phi_{10}=0\\
\phi_2+\phi_8+\phi_9-\phi_5-\phi_6=0,\ \phi_3-\phi_8-\phi_9=0\\
\phi_{11}+\phi_{15}-\phi_1=0,\ \phi_{13}-\phi_3-\phi_{12}=0\\
\phi_{12}+\phi_{14}-\phi_2-\phi_{11}=0\\
\phi_4(R_{\mathrm{shell}}+R_m+R_{\mathrm{pm}})+\phi_7R_L-\mathrm{NI}-F_{\mathrm{pm}}=0\\
\phi_{10}R_{\mathrm{base}}+\phi_1R_{\mathrm{rod1}}+\phi_{15}(R_{s12}+R_{\mathrm{AG3}})-\phi_7R_L=0\\
\phi_5R_1+\phi_2R_{\mathrm{rod2}}-\phi_1R_{\mathrm{rod1}}-\phi_{11}R_3=0\\
\phi_3R_{\mathrm{rod3}}+\phi_9R_2-\phi_2R_{\mathrm{rod2}}-\phi_{12}R_4=0\\
\phi_{11}R_3+\phi_{14}(R_{s22}+R_{\mathrm{AG4}})-\phi_{15}(R_{s12}+R_{\mathrm{AG3}})=0\\
\phi_{12}R_4+\phi_{13}R_{\mathrm{or}}-\phi_{14}(R_{s22}+R_{\mathrm{AG4}})=0\\
\phi_8(R_{s21}+R_{\mathrm{AG2}})-\phi_9R_2=0\\
\phi_6(R_{s11}+R_{\mathrm{AG1}})-\phi_5R_1=0
\end{cases} \tag{16}$$

Appendix B

The matrix $\boldsymbol{\phi}$, $\boldsymbol{A}$, and $\boldsymbol{B}$ in (1) is as follows: (17) shown at the top of this page.

References

[1] H. C. Mongia, T. J. Held, G. C. Hsiao, and R. P. Pandalai, "Challenges and progress in controlling dynamics in gas turbine combustors," *J. Propulsion Power*, vol. 19, pp. 822–829, 2003.

[2] O. Dessens, M. O. Köhler, H. L. Rogers, R. L. Jones, and J. A. Pyle, "Aviation and climate change," *Transport Policy*, vol. 34, pp. 14–20, 2014.

[3] L. Li, Y. Lin, Z. Fu, and C. Zhang, "Emission characteristics of a model combustor for aero gas turbine application," *Exp. Thermal Fluid Sci.*, vol. 72, pp. 235–248, 2016.

[4] M. Shehata, "Emissions and wall temperatures for lean prevaporized premixed gas turbine combustor," *Fuel*, vol. 88, no. 3, pp. 446–455, 2009.

[5] X. Han *et al.*, "Inlet temperature driven supercritical bifurcation of combustion instabilities in a lean premixed prevaporized combustor," *Exp. Thermal Fluid Sci.*, vol. 109, 2019, Art. no. 109857.

[6] C. Ruan *et al.*, "Experimental study on combustion stability characteristics in liquid-fueled gas turbine model combustor: Fuel sensitivities and flame/flow dynamics," *Fuel*, vol. 265, 2020, Art. no. 116973.

[7] T. Poinsot, "Prediction and control of combustion instabilities in real engines," *Proc. Combustion Inst.*, vol. 36, no. 1, pp. 1–28, 2017.

[8] Y. Liu, J. Li, T. Zhang, and Y. Yan, "Active suppression of swirl-stabilized combustion instability," *Fuel*, vol. 287, 2021, Art. no. 119559.

[9] A. Morgans and A. Dowling, "Model-based control of combustion instabilities," *J. Sound Vib.*, vol. 299, no. 1, pp. 261–282, 2007.

[10] S. Tachibana, L. Zimmer, Y. Kurosawa, and K. Suzuki, "Active control of combustion oscillations in a lean premixed combustor by secondary fuel injection coupling with chemiluminescence imaging technique," *Proc. Combustion Inst.*, vol. 31, no. 2, pp. 3225–3233, 2007.

[11] J. P. Hathout, M. Fleifil, A. M. Annaswamy, and A. F. Ghoniem, "Combustion instability active control using periodic fuel injection," *J. Propulsion Power*, vol. 18, no. 2, pp. 390–399, 2002.

[12] C. Hantschk, J. Hermann, and D. Vortmeyer, "Active instability control with direct-drive servo valves in liquid-fueled combustion systems," *Symp. (Int.) Combustion*, vol. 26, no. 2, pp. 2835–2841, 1996.

[13] S. Feng and J. Li, "H loop-shaping control of azimuthal combustion instabilities in annular combustors," *J. Low Freq. Noise, Vib. Act. Control*, vol. 40, no. 1, pp. 395–412, 2021.

[14] J. Rubio-Hervas, M. Reyhanoglu, and W. MacKunis, "Observer-based sliding mode control of Rijke-type combustion instability," *J. Low Freq. Noise, Vib. Act. Control*, vol. 34, no. 2, pp. 201–217, 2015.

[15] N. Docquier and S. Candel, "Combustion control and sensors: A review," *Prog. Energy Combustion Sci.*, vol. 28, no. 2, pp. 107–150, 2002.

[16] J. DeLaat, K. Breisacher, J. Saus, and D. Paxson, "Active combustion control for aircraft gas turbine engines," in *Proc. 36th AIAA/ASME/SAE/ASEE Joint Propulsion Conf. Exhibit.*, 2000, Art. no. 3500.

[17] Y. Yuan, T. Zhang, Z. Lin, and J. Zhang, "An investigation into factors determining the metering performance of a fuel control unit in an aero engine," *Flow Meas. Instrum.*, vol. 71, 2020, Art. no. 101672.
[18] M. Montazeri-Gh, M. Nasiri, M. Rajabi, and M. Jamshidfard, "Actuator-based hardware-in-the-loop testing of a jet engine fuel control unit in flight conditions," *Simul. Model. Pract. Theory*, vol. 21, no. 1, pp. 65–77, 2012.
[19] H. Nabae and T. Higuchi, "A novel electromagnetic actuator based on displacement amplification mechanism," *IEEE/ASME Trans. Mechatron.*, vol. 20, no. 4, pp. 1607–1615, Aug. 2015.
[20] H. Guo, D. Wang, and J. Xu, "Research on a high-frequency response direct drive valve system based on voice coil motor," *IEEE Trans. Power Electron.*, vol. 28, no. 5, pp. 2483–2492, May 2013.
[21] Y. Zhu and L. Ji, "Theoretical and experimental investigations of the temperature and thermal deformation of a giant magnetostrictive actuator," *Sensors Actuators A: Phys.*, vol. 218, pp. 167–178, 2014.
[22] Y. Zhu, X. Yang, and T. Fu, "Dynamic modeling and experimental investigations of a magnetostrictive nozzle-Flapper servovalve pilot stage," *Proc. Inst. Mech. Eng., Part I: J. Syst. Control Eng.*, vol. 230, no. 3, pp. 244–254, 2016.
[23] Y. Guo *et al.*, "Model and experimental research of a hybrid self-contained electro-hydrostatic actuator using piezoelectric stack," *J. Intell. Mater. Syst. Structures*, vol. 29, no. 7, pp. 1348–1359, 2018.
[24] N. H. Schiller, W. R. Saunders, W. A. Chishty, U. Vandsburger, and W. T. Baumann, "Development of a piezoelectric-actuated fuel modulation system for active combustion control," *J. Intell. Mater. Syst. Struct.*, vol. 17, no. 5, pp. 403–410, 2006.
[25] H. Li, J. Liu, K. Li, J. Deng, and Y. Liu, "Development of a high differential pressure piezoelectric active proportional regulation valve using a bending transducer," *IEEE Trans. Ind. Electron.*, vol. 68, no. 12, pp. 12513–12523, Dec. 2021.
[26] S. Chakrabarti and M. J. Dapino, "A dynamic model for a displacement amplified magnetostrictive driver for active mounts," *Smart Mater. Struct.*, vol. 19, no. 5, 2010, Art. no. 055009.
[27] L. Lai and Z. Zhu, "Design, modeling and testing of a novel flexure-based displacement amplification mechanism," *Sensors Actuators A: Phys.*, vol. 266, pp. 122–129, 2017.
[28] Y. Tian *et al.*, "A spatial deployable three-DOF compliant nano-positioner with a three-stage motion amplification mechanism," *IEEE/ASME Trans. Mechatron.*, vol. 25, no. 3, pp. 1322–1334, Jun. 2020.
[29] Z. Yang *et al.*, "Dynamic analysis and application of a novel hydraulic displacement amplifier based on flexible pistons for micro stage actuator," *Sensors Actuators A: Phys.*, vol. 236, pp. 228–246, 2015.
[30] P. Bartlett, S. Eaton, J. Gore, W. Metheringham, and A. Jenner, "High-power, low frequency magnetostrictive actuation for anti-vibration applications," *Sensors Actuators A: Phys.*, vol. 91, no. 1, pp. 133–136, 2001.
[31] L. Chen, Y. Zhu, J. Ling, and Z. Feng, "Development and test of a two-dimensional stacked terfenol-d actuator with high bandwidth and large stroke," *IEEE/ASME Trans. Mechatron.*, vol. 26, no. 4, pp. 1951–1959, Aug. 2021.
[32] R. Li, Y. Zhu, R. Wang, Y. Li, and B. Niyomwungeri, "Design and analysis of a nested structure micro-displacement amplification mechanism for a galfenol-based actuator," *Smart Mater. Structures*, vol. 28, no. 9, 2019, Art. no. 095026.
[33] Y. Zhu, X. Yang, and N. M. Wereley, "Research on hysteresis loop considering the prestress effect and electrical input dynamics for a giant magnetostrictive actuator," *Smart Mater. Structures*, vol. 25, no. 8, 2016, Art. no. 085030.

Long Chen received the B.S. degree in mechanical engineering from the School of Mechanical Engineering, Jiangsu University, Zhenjiang, China, in 2018. He is currently working toward the Ph.D. degree in mechanical engineering with the Nanjing University of Aeronautics and Astronautics, Nanjing, China.

His research interests include mechanical design and control of magnetostrictive actuators.

Yuchuan Zhu received the Ph.D. degree in mechanical engineering from the Nanjing University of Science and Technology, Nanjing, China, in 2007.

In 2007, he joined the Nanjing University of Aeronautics and Astronautics, Nanjing, China, where he is currently a Full Professor with the Department of Mechanical and Electronic Engineering, College of Mechanical and Electrical Engineering. From 2014 to 2016, he was a Senior Visiting Scholar Fellow with the Department of Aeronautics and Astronautics, University of Maryland, College Park, MD, USA. He has authored or coauthored more than 70 peer-reviewed papers in the areas of intelligent materials and structures, electrohydraulic servo valves, and electro-hydraulic actuators. His current research interests include intelligent materials and intelligent structures, advanced aviation hydraulics, electrohydraulic servo valves, and hydraulic simulation.

Jie Ling (Member, IEEE) received the B.S. and Ph.D. degrees in mechanical engineering from the School of Power and Mechanical Engineering, Wuhan University, Wuhan, China, in 2012 and 2018, respectively.

From August 2017 to November 2017, he was a Visiting Ph.D. Student with the Department of Automatic Control and Micro-Mechatronic Systems, FEMTO-St Institute, Besançon, France. From January 2019 to January 2020, he was a Postdoctoral Research Fellow with the Department of Biomedical Engineering, National University of Singapore, Singapore. Since August 2020, he has been an Associate Research Fellow with the College of Mechanical and Electrical Engineering, Nanjing University of Aeronautics and Astronautics, Nanjing, China. His research interests include mechanical design and precision motion control of piezoelectric nanopositioning systems and micromanipulation robots.

Mingming Zhang received the B.S. degree in mechanical engineering in 2020 from the College of Mechanical and Electrical Engineering, Nanjing University of Aeronautics and Astronautics, Nanjing, China, where she is currently working toward the Ph.D. degree in mechanical engineering.

Her research interests include mechanical design and control of smart material-based electro-hydrostatic actuator.